Improving Cryogenic DT Implosion Performance on OMEGA

Introduction

Layered cryogenic deuterium–tritium (DT) capsules are being imploded on LLE's 60-beam OMEGA Laser System[1] to demonstrate hydrodynamic performance equivalent to that of a symmetric direct-drive target designed to ignite with the laser energy available at the National Ignition Facility (NIF).[2] Hydrodynamic equivalence implies that the shell velocity at the end of acceleration (typically referred to as the implosion velocity or V_{imp}), the in-flight aspect ratio (IFAR, defined as the ratio of the shell radius and the shell thickness evaluated after the shell has imploded to 2/3 of its initial radius), and the peak laser drive intensity (I_{L}) are the same as those of a symmetric ignition design[3] for the NIF. The demonstration of direct-drive hydrodynamic equivalence is viewed as an important scientific prerequisite for a polar-drive (PD)–ignition campaign on the NIF later in this decade.[4]

The polar-drive concept[5] was developed in 2004 to provide a platform for directly driven implosions on the NIF while the facility is configured for x-ray drive. A preliminary assessment of PD hot-spot target designs has shown that direct-drive ignition might be achieved on the NIF with a laser energy as low as 1 MJ_{UV} (Ref. 6). The experimental plan to support the PD-ignition campaign is based on the validation of symmetric direct-drive performance modeling (laser coupling,[7–10] shock timing[11] and thermal transport,[12,13] hot-electron generation,[14] and adiabat control[15]) using cryogenic layered DT implosions on OMEGA. Additionally, select 40-beam, ambient gas-filled PD implosions are being used to confirm drive symmetry modeling.[16] Therefore, PD-ignition designs for the NIF will be based on physics models embedded in the radiation–hydrodynamic design codes that have been validated against symmetric direct-drive–implosion data.

The cryogenic implosion database at the Omega Laser Facility includes over 270 layered fuel implosions [roughly half using pure deuterium (D_2) fuel and half using DT]. The first cryogenic D_2 capsule implosions[17] were performed in 2000 and cryogenic DT implosions[18] began in late 2006. Among the highlights of these experiments was the demonstration of areal densities in D_2 fuel in excess of 200 mg/cm^2 (Refs. 12 and 19), the demonstration of areal densities in DT fuel of 300 mg/cm^2 (Refs. 3 and 20) (nominally the minimum areal density needed to sustain a thermonuclear burn wave), and the demonstration of yields relative to 1-D predictions in excess of 15% (Ref. 21).

This article describes recent progress toward demonstrating ignition hydrodynamically equivalent implosion performance on OMEGA. The following sections (1) discuss the concept of hydrodynamic similarity and the requirements for OMEGA target design; (2) present and discuss the data from a series of cryogenic DT implosions spanning a design space that includes ignition, concluding that target performance on OMEGA is impacted by capsule surface perturbations leading to ablator mixing into the hot spot; (3) discuss the origin and hydrodynamic modeling of these capsule surface perturbations; and (4) plot all of the cryogenic DT data using the experimental ignition threshold factor (ITFx) formalism described in Ref. 22 scaled appropriately for the target mass and laser-energy differences between OMEGA and the NIF. The ITFx formalism is a convenient metric for comparing relative target performance across a broad design space and is related to the generalized Lawson criterion applied to inertial confinement fusion (ICF) derived by Betti *et al.*[23] Final concluding remarks are given in the last section.

Hydrodynamic Similarity and Experimental Design

Hydrodynamic similarity can be used to extrapolate implosion performance from the 26-kJ_{UV} OMEGA to the 1.8-MJ_{UV} NIF laser. In this way, implosions can be performed on OMEGA to probe the design space for targets on the NIF. In Ref. 24, Betti *et al.* showed explicitly that an ignition design for the NIF based on a specific adiabat (α, defined as the ratio of the shell pressure to the Fermi-degenerate pressure), implosion velocity, and laser intensity can be reproduced on OMEGA with the same adiabat, implosion velocity, and laser intensity. While this scaling should lead to the same peak stagnation pressure and density in the OMEGA and NIF cores, the resulting yields and fuel areal density will necessarily be lower on OMEGA because of the smaller fuel mass and laser energy. Indeed, for

hydrodynamic similarity, the target mass must scale as the laser energy E_L, the target radius as $E_L^{1/3}$, the laser power as $E_L^{2/3}$, and the laser pulse length as $E_L^{1/3}$.

The assumption implicit in the hydro scaling argument is that the ablation pressure and preheat sources are independent of target scale (and facility). This is unlikely to be the case, however, since the coronal plasma scale length on the NIF relative to OMEGA will scale as the radius of the capsule (approximately 4× longer) for hydrodynamically similar implosions. The longer plasma scale lengths will reduce the ablation pressure via light-scattering losses and increased cross-beam energy transfer (CBET)[8] and increase the production of hot electrons (and potentially fuel preheating) from the two-plasmon–decay (TPD) instability.[14,25] Although these laser–plasma instabilities do not *a priori* restrict the design space available on OMEGA for ignition-relevant implosions, they may limit the penultimate performance that can be achieved.

The cryogenic target design for the experiments discussed here is shown in Fig. 135.1. This design is scaled from the 1.5-MJ symmetric direct-drive–ignition design published by Goncharov *et al*. in 2010 (Ref. 3). The capsule ablator material [Fig. 135.1(a)] is pure CD (deuterated plastic) or CD doped with a few atom percent of silicon (the dopant tailors the adiabat at the ablation surface to reduce the imprint growth rate[7]). The peak intensity of the triple-picket drive pulse [Fig. 135.1(b)] is 9×10^{14} W/cm^2; the total drive energy is designed to be 26 kJ. The capsule radius is nominally 430 μm, which is $(1.5\ \text{MJ}/0.026\ \text{MJ})^{1/3} \sim 3.9\times$ smaller than the 1.5-MJ ignition design (1700 μm).

Based on the hydrodynamic similarity argument above, this target platform can be used to access a broad region of design space that includes the 1.5-MJ ignition design. With constant drive intensity and laser energy, the V_{imp} and IFAR are varied by changing the thickness of the ablator and DT ice layer and adjusting the picket energies and temporal spacing to achieve the desired adiabat at the inner fuel surface (the picket adjustments are used to ensure the correct shock timing and radial convergence). Figure 135.2 is a scatter plot in IFAR and adiabat space of recent cryogenic DT capsule implosions on OMEGA (i.e., each point represents an implosion on OMEGA with the indicated adiabat and IFAR). These implosions were selected from a set of over 60 experiments (performed over the past 18 months) based on a set of "physics quality" criteria that include target alignment at shot time (within 15 μm of target chamber center), ice-layer quality [less than 2-μm root mean square (rms) over all modes], and pulse-shape quality (typically picket energies within 10% of the design specification). The shaded region for

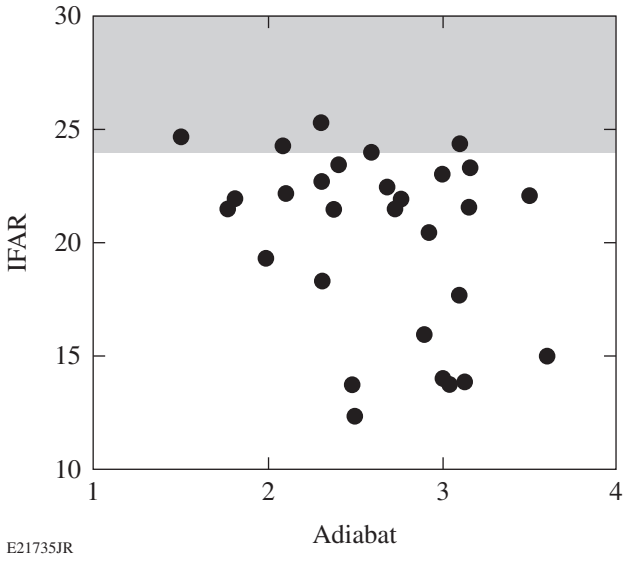

Figure 135.2
A scatter plot in IFAR–adiabat design space of 29 cryogenic DT implosions on OMEGA. Each black circle represents an implosion with the specific post-shot calculated values of IFAR and adiabat. The shaded region represents the ignition-relevant region of this design space. IFAR: in-flight aspect ratio.

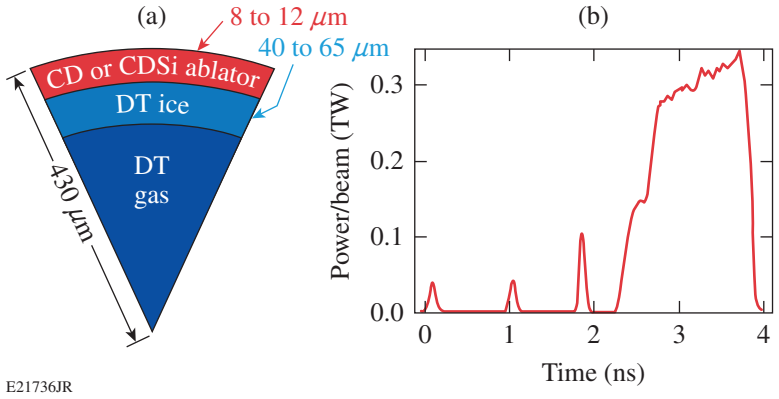

Figure 135.1
(a) The standard cryogenic DT capsule imploded on OMEGA consists of a thin CD or doped-CD ablator fill with several hundred atm of DT gas to create a 40- to 60-μm-thick ice layer. (b) The standard 25-kJ drive pulse consists of a series of three pickets used to establish the shell adiabat and control shock coalescence and a high-intensity main drive.

IFAR > 23 shows the approximate design space for ignition with implosion velocities between 350 and 400 km/s.

Figure 135.1(a) shows the range of ablator and ice thickness used for the points shown in Fig. 135.2. The implosion velocities range from 250 km/s to 380 km/s (e.g., a 9.2-μm CD ablator with an ice layer of 48 μm is predicted to achieve a $V_{\rm imp}$ of 350 km/s). Although the adiabat, IFAR, and $V_{\rm imp}$ are calculated quantities [based on the one-dimensional (1-D) design code *LILAC*[26]], the $V_{\rm imp}$ is confirmed experimentally by measuring the implosion burn history using the neutron temporal diagnostic (NTD).[27] *LILAC* incorporates nonlocal thermal transport[12] and a stimulated Brillouin scattering (SBS) model[8] to account for cross-beam energy transfer. A 10% change in the predicted velocity is a timing shift of 150 ps in the NTD. The absolute temporal accuracy of the NTD is 25 ps, so the implosion velocity is known to within a few percent.

Measurements and Discussion

The ICF Lawson criterion[23] can be used to connect the design parameters $V_{\rm imp}$, adiabat, and IFAR to the experimentally measured observables. These observables include the primary neutron yield $Y_{\rm n}$, the compressed fuel areal density ρR, the hot-spot ion temperature $T_{\rm ion}$, the absorbed laser energy, and the neutron burn history. The Lawson criterion is defined as $\chi = P\tau/P\tau(T)_{\rm ign} > 1$ (Ref. 28), where P is the plasma pressure and τ is the energy confinement time. In Ref. 28, Betti *et al.* derived an approximate 1-D ignition parameter based on the generalized Lawson criterion

$$\chi(\text{1-D}) \sim \left(\rho R^{\text{no}\,\alpha}\right)^{0.8} \times \left(T_{\rm ion}^{\text{no}\,\alpha}/4.4\right)^{1.8} > 1, \qquad (1)$$

where $T_{\rm ion}$ is given in keV and ρR in g/cm^2. The superscript "no α" indicates that alpha-particle energy deposition is turned off in the 1-D simulations used to validate the analytic scaling. Recognizing that implosion nonuniformities significantly degrade 1-D performance, the authors used a simple three-dimensional (3-D) burn model to derive a generalized Lawson criterion

$$\chi(\text{3-D}) \sim \left(\rho R^{\text{no}\,\alpha}\right)^{0.8} \times \left(T_{\rm ion}^{\text{no}\,\alpha}/4.4\right)^{1.8} \times \text{YOC}_{\text{3-D}}^{m}. \qquad (2)$$

$\text{YOC}_{\text{3-D}}$ is the ratio of the estimated 3-D yield to the predicted 1-D yield and m is analytically given as 0.64 but is between 0.4 and 0.5 based on fitting simulation yields with an ignition criterion of $\chi \sim 1$. It is difficult to use this form of χ to evaluate absolute implosion performance given the dependence on simulations and the measured $T_{\rm ion}$, which is sensitive to fuel motion. Therefore, Betti *et al.*[24] modified Eq. (2) to remove the explicit dependence on the YOC and replace the $T_{\rm ion}$ with the absolute yield $Y_{\rm n}$. This version of the "measurable" generalized Lawson criterion for ICF is given by

$$\chi \sim \left(\rho R^{\text{no}\,\alpha}\right)^{0.61} \times \left(0.24\, Y_{\rm n}/M_{\rm fuel}\right)^{0.34}, \qquad (3)$$

where ρR is in g/cm^2, $Y_{\rm n}$ is in units of 10^{16}, and the fuel mass $M_{\rm fuel}$ is in mg. This form of χ depends only on the measured fuel ρR and the neutron yield and is roughly equivalent to the cube root of the experimental ignition threshold factor (ITFx) derived by Haan *et al.*[22]

It has been shown[24] that ignition hydrodynamically equivalent implosions on OMEGA occur for values of $\chi \gtrsim 0.16$. This can be satisfied for a range of areal densities and yields. Given that a ρR of ~300 mg/cm^2 has already been demonstrated on OMEGA,[3,20] a $\chi \sim 0.16$ corresponds to a yield of 4×10^{13}. These values of $Y_{\rm n}$ and ρR provide a convenient metric for demonstrating ignition hydrodynamically equivalent implosion performance with symmetric direct drive on OMEGA and are consistent with an earlier analysis discussed in Ref. 20.

Figure 135.3 shows the dependence of the 1-D fractional measured ρR ($\rho R/\rho R_{\text{1-D}}$) as a function of the calculated fuel adiabat [Fig. 135.3(a)] and IFAR [Fig. 135.3(b)] for the database shown in Fig. 135.2. As expected, the fraction of the 1-D ρR produced in the implosions is lower for higher-convergence, lower-adiabat implosions. The trend of lower ρR with decreasing shell stability is also clear as a function of IFAR. The measured fraction of the 1-D ρR approaches 80% for values of the adiabat above ~2.5 and values of IFAR below ~20 (note that

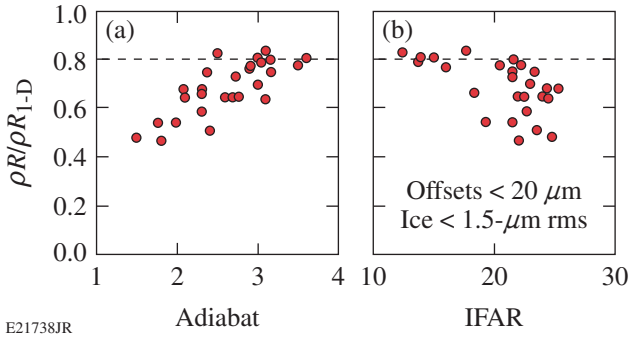

Figure 135.3
(a) The correlation between the ratio of the measured and 1-D–predicted areal density and the calculated adiabat for the implosions in Fig. 135.2 shows a drop in the measured ρR for adiabats generally less than 2.5. (b) The correlation between the ratio of the measured and 1-D–predicted areal density and the calculated IFAR for the implosions in Fig. 135.2 shows a drop in the measured ρR for IFAR's generally greater than 17.

the velocities for the implosions at these lower adiabats range from 280 to 320 km/s). Burn truncation[29] and ^{3}He buildup in the capsule caused by tritium β-decay can account for much of the degradation relative to the prediction. Estimates of the void pressure resulting from the buildup of ^{3}He are sufficient to cause a degradation of the predicted ρR of 10% to 15%. The 1-D prediction for the points in Fig. 135.3 does not take into account the increased pressure in the capsule related to ^{3}He buildup as the target ages.

The ρR measurements in Fig. 135.3 were obtained with two independent instruments: the magnetic recoil spectrometer (MRS)[30] and a highly collimated neutron time-of-flight (nTOF) detector.[31] The areal density inferred from the nTOF is based on a different part of the (n,T/D) scattering cross section[32] than that used in the reduction of the MRS data. While the MRS measures the fraction of the primary yield forward scattered by the compressed DT, the nTOF measures the (n,T) backscatter edge at 3.5 MeV to infer the triton density in the compressed fuel. The systematic error on the ρR inferred from the nTOF is somewhat higher (estimated to be <15%) than that from the MRS (6%). However, where both measurements are available (a small number of the experiments did not have the nTOF available), the value of the ρR used in Fig. 135.3 (and subsequent analyses) is the average of the two measurements.

Figure 135.4 is a duplicate of Fig. 135.2 with contours of constant $\rho R/\rho R_{1\text{-D}}$ based on the same database of shots. In this two-dimensional (2-D) design space, a stability boundary suggested by Figs. 135.3(a) and 135.3(b) is clearly evident. For this set of experiments, the edge of the boundary can be roughly defined as IFAR = $20(\alpha/3)^{0.8}$. While Fig. 135.3(b) suggests that the measured ρR begins to deviate from the 1-D prediction for values of IFAR > 17, the 2-D contour plot clearly shows that the 1-D ρR is recovered for larger IFAR as long as the adiabat is suitably large. This further confirms that the stability of these targets is sensitive to design details that can be fully accessed based on the flexibility of the target platform.

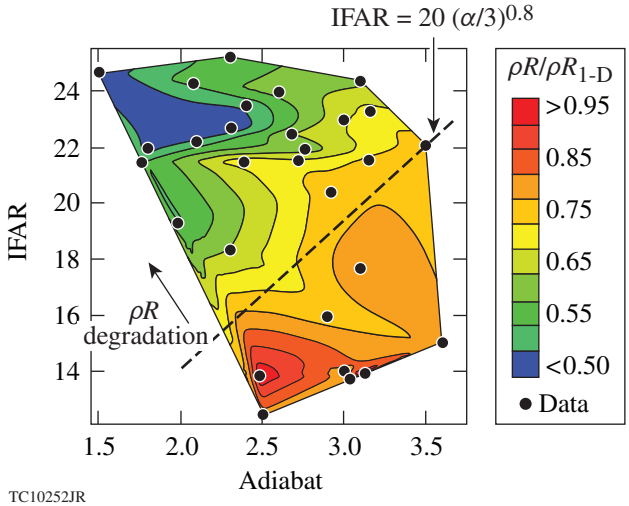

Figure 135.4
Contours of the measured areal-density fraction relative to 1-D prediction ($\rho R/\rho R_{1\text{-D}}$) show a steep drop for values of the IFAR above the line defined by $20(\alpha/3)^{0.8}$.

Figure 135.5 shows the measured (red circles) and 1-D–predicted (black circles) Y_n [Fig. 135.5(a)] and T_{ion} [Fig. 135.5(b)]

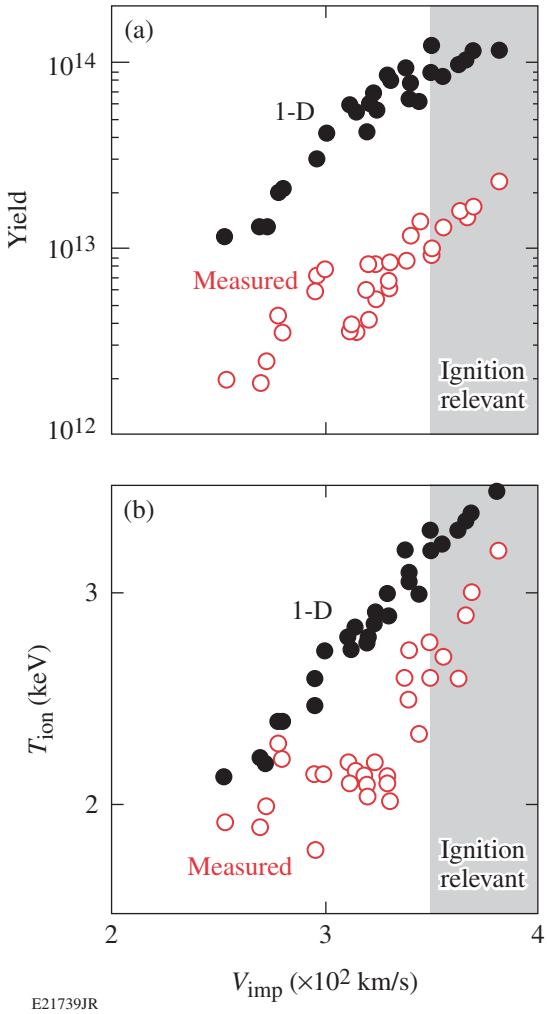

Figure 135.5
(a) The predicted 1-D and measured yields increase with increasing implosion velocity. The adiabat was increased to reach implosion velocities above 330 km/s. (b) While the 1-D ion temperature increases linearly with the implosion velocity, the measured temperature is fairly constant until the implosion velocity exceeds 330 km/s. The shaded regions indicate ignition-relevant implosion velocities.

as functions of the calculated implosion velocity. The measured yield increases uniformly with implosion velocity from 250 km/s to 380 km/s. The larger spread in the experimental yields for $V_{imp} \sim 300$ to 320 km/s suggests that the shell is becoming increasingly unstable as the implosion velocity is increased. The data points at higher V_{imp} were therefore acquired using a higher fuel adiabat to stabilize perturbation growth at the ablation surface and the ice–gas interface. This additional stabilization is clearly evident in Fig. 135.5(b), where there is little variation in the measured T_{ion} with increasing V_{imp} until the fuel adiabat is raised to access V_{imp} above ~320 km/s. With the higher-adiabat implosions, T_{ion} increases rapidly with V_{imp} reaching 90% to 95% of the prediction at 380 km/s.

Figure 135.6 is a duplicate of Fig. 135.2 with contours of constant $Y_n / Y_{n_{1\text{-D}}}$ [this is the ratio of the measured and simulated yields from Fig. 135.5(a), commonly referred to as YOC]. The vertical contours indicate that the measured yield depends primarily on the adiabat for values of IFAR < 20 to 22. Only at the highest adiabat does the yield appear to be independent of IFAR for ignition-relevant values (a target is unlikely to ignite at these adiabats with the energy available on the NIF). The YOC for these few data points is >20%. The YOC for ignition-relevant values of the adiabat and IFAR is generally less than 10%.

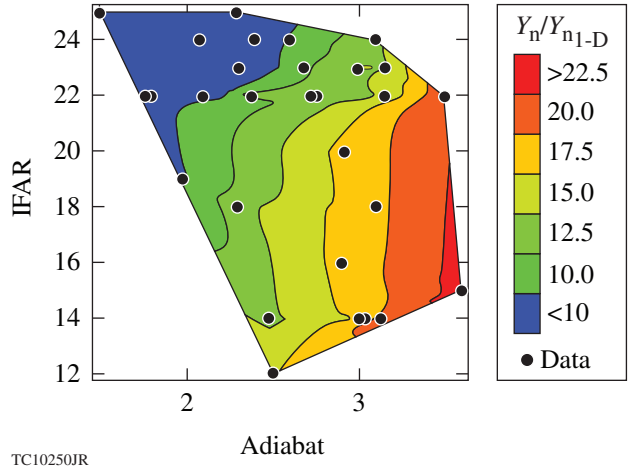

Figure 135.6
Contours of the measured yield fraction relative to 1-D predictions [yield-over-clean (YOC)] show that the yield depends primarily on the adiabat for IFAR's generally less than 20.

The largest value of χ [Eq. (3)] in this data set is 0.09. For this shot (and several others in the 0.08 range), the values of the measured ρR and Y_n are approximately half of the values needed to demonstrate ignition hydrodynamically equivalent implosion performance. These highest-performing implosions are not associated with ignition-relevant values of IFAR and adiabat. This is seen in Fig. 135.7, where contours of constant $\chi/\chi_{1\text{-D}}$ are plotted in the IFAR–adiabat space of Fig. 135.2. The contours clearly show that relative to 1-D prediction, target performance decreases with increasing IFAR and decreasing adiabat. Not surprisingly, this is consistent with the stability boundary identified in Fig. 135.4.

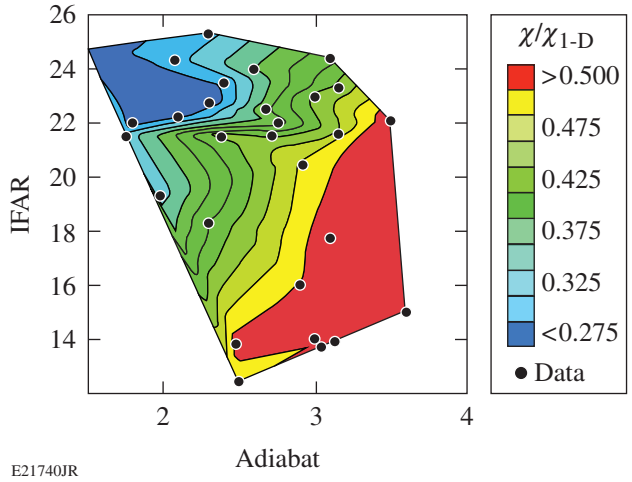

Figure 135.7
Contours of the measured χ fraction relative to the 1-D–predicted χ show a steep drop with increasing IFAR for ignition-relevant adiabats (<2.5).

Together, these data suggest that as the design approaches ignition hydrodynamic equivalence, the fuel shell breaks apart during acceleration, leading to a drop in the burn-averaged fuel areal density. The subsequent loss in the hot-spot pressure and temperature leads to a drop in the primary yield. The shell breakup during acceleration suggests Rayleigh–Taylor (RT) perturbation growth from the ablation surface (as opposed to deceleration-driven growth at the ice–gas interface). Such growth would be expected to mix ablator material into the core. This mixing is confirmed in Fig. 135.8, where the yield-normalized x-ray emission from the core is plotted as a function of the adiabat. The yield normalization factor comes from a fit of the 1-D–predicted x-ray emission. When normalized to $Y_{1\text{-D}}^{0.57}$, simulated core x-ray emission is approximately constant for all of the experiments. This is shown by the black circles in Fig. 135.8. If carbon mixing enhances the core emission, this should be evident when the experimental x-ray emission is normalized to $Y_{meas}^{0.57}$. These values are plotted as the red squares. The data clearly show that when the adiabat is less than 2.5, the core x-ray emission is strongly enhanced relative to the high-adiabat experiments, whereas Figs. 135.4 and 135.6 show that the shell is likely integral through acceleration. The

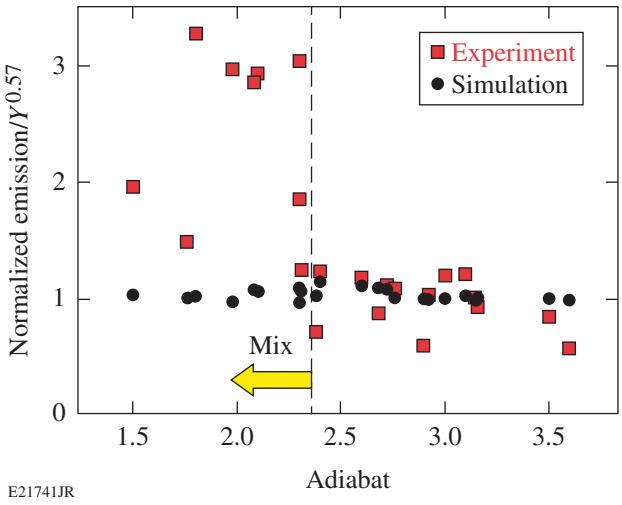

Figure 135.8
The yield-normalized x-ray emission from 1-D simulations (black circles) and cryogenic DT implosions (red squares) is plotted as a function of the implosion adiabat. The experimental points show a pronounced increase in the x-ray emission relative to 1-D prediction for adiabats generally less than 2.5, indicating that this emission may be due to higher-Z carbon mixing into the core.

normalization of the experimental and simulated points at high adiabats is arbitrary, as are the units of the normalized emission. The simulated x-ray emission used to establish the yield normalization is restricted to the sensitivity range of the gated x-ray imager used for the measurement (roughly 4 to 7 keV).

Capsule Surface Quality and 2-D Simulations

As discussed in **Measurements and Discussion** (p. 147), the accumulated data suggest a high level of ablator mixing into the hot spot at peak burn. This level of mix would require a significant source of perturbations on the capsule surface to drive CD into the core before stagnation. The shadowgraphy-based imaging system used to characterize the ice-layer quality was refocused to image the capsule surface. Figure 135.9 shows a stitched image in pixel space of five capsule surface images acquired at the same focal depth as the target was rotated. The stitched image contains about 2/3 of the capsule surface and shows dozens of surface "defects" distributed randomly (there is no discernible pattern from one target to another) across the surface.

A detailed optical analysis of these defects confirms that most of the features reside on the outer capsule surface and originate during the high-pressure fill and cooling cycle (Ref. 18 describes the permeation filling process and the DT layering/characterization in detail), i.e., the features do not correspond with fabrication defects identified prior to the fill. A subset of the filled capsules has a small number of dendritic defects on the inner surface of the CD shell. An analysis of one of these inner surface dendritic defects following a controlled depressurization of a filled capsule showed that the radial depth is of the order of 0.1 μm or less, within the smoothness specification for the capsule.

Every target imploded on OMEGA since January 2012 has had the surface defects analyzed based on images such as the one shown in Fig. 135.9. The analysis identifies the type of defect (outer surface or inner surface) and the defect area. Figure 135.10(a) is a plot of the defect-size distribution for the targets filled in 2012 (48 total). The average defect size is ~140 μm^2; the imaging system is capable of resolving features with an area as small as 20 μm^2. Figure 135.10(b) shows a histogram of the target defect frequency distribution (bin size is ten defects). The defect count can exceed 100 on a single target. The total defect area for the targets discussed in this article ranged from a few thousand up to 15,000 μm^2 (nearly 1% of the total capsule surface area). The variation in defect count and total area from target to target and fill to fill is not understood.

Two-dimensional simulations of a single isolated surface defect suggest that the defects account for much of the observed target performance degradation relative to 1-D prediction. The implosion performance of several targets was simulated by assuming a uniform distribution of constant-size defects

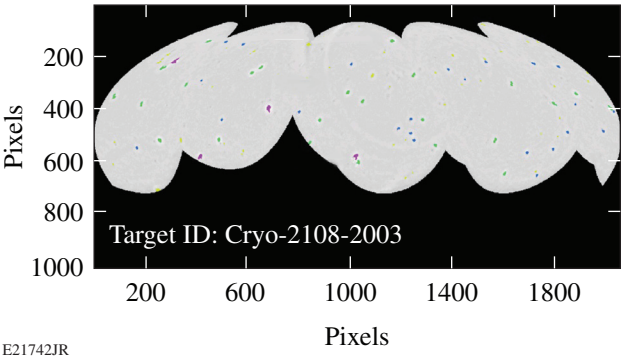

Figure 135.9
A stitched set of images of a cryogenic DT capsule surface during characterization. The image shows dozens of surface defects associated with the high-pressure DT permeation fill. The defects are likely frozen gas contaminants in the DT fuel.

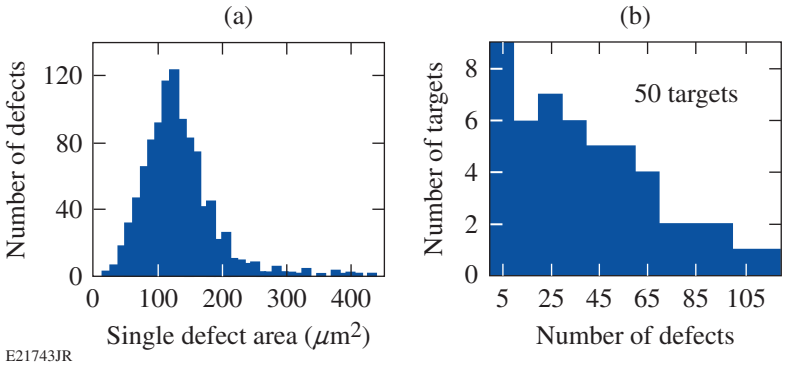

Figure 135.10
(a) The defect-size distribution for the targets characterized in 2012 show that the average defect size is about 140 μm^2. (b) The frequency distribution of the defects on 50 targets filled and characterized in 2012. Most targets have several dozen individual defects.

(80 μm^2) with a thickness of 1 μm. The thickness of the defects cannot be measured with the optical imaging system used to characterize the DT ice layer (limited spatial resolution and contrast) unless they can be resolved on the limb of the images. In some cases this has been possible; however, most of the defects cannot be identified on the limb of the capsule images. A thickness of 1 μm was used in the simulations as a compromise: some will be larger while most are smaller. A 2-D simulation with a single defect and reflecting boundary conditions was performed using a sector defined as $4\pi/N$, where N is the number of defects on the target. The reflecting boundaries mimic the presence of neighboring defects in this simplified 2-D simulation. Assuming that the defects are identical and uniformly distributed around a target, the predicted yield is then N times the results of the simulation. The simulated ion temperature and neutron-averaged ρR are taken as the average for the target. Table 135.I shows the results for shot 66999 (August 2012). The first row is the 1-D prediction using *LILAC* with nonlocal (NL) thermal transport and an SBS model to account for CBET in the absorbed energy.[8] The second row is the 2-D simulation described above including single-beam laser imprint[33] but no isolated defects. The third row is the 2-D simulation including the average isolated defect with N = 150. The fourth row is the experimentally measured values. The isolated defect simulation reproduces the experimental measurements reasonably well, while the imprint-only simulations cannot explain the observed implosion performance. The other simulated implosions show a quantitatively similar behavior with respect to measured target performance. While the number of defects simulated was larger than the average number shown in Fig. 135.10(b) and the area of each defect was less than the average shown in Fig. 135.10(a), the total defect area was similar to the average of most targets in the 2012 database. The key point is that injecting the proper amount of ablator material into the core via ablation-front RT growth reproduces the experimental performance observables.

Table 135.I: For shot 66999, the results of 1-D simulations including nonlocal thermal transport and cross-beam energy transfer, 2-D simulations with imprint, and 2-D simulations based on an isolated surface defect are compared with the measured yield, areal density, and ion temperature.

Shot 66999	Y_n ($\times 10^{13}$)	ρR (mg/cm^2)	T_{ion} (keV)
1-D (NL + SBS)	7.9	238	3.1
2-D imprint	4.5	242	3.4
2-D defect	1.8	151	2.7
Measured	1.2	175	2.5

Further progress toward the demonstration of ignition hydrodynamically equivalent implosion performance requires that these isolated defects be eliminated from the capsules. Few, if any, of these defects are particulate in nature. Steps taken in 2011 eliminated the identified sources for particulate debris. The defects are condensed non-hydrogenic gases entrained in the closed DT-fuel supply; analysis confirms that the fuel supply contains nearly 0.5% organics and hundreds of ppm of nitrogen, water, and CO_2. The organics are likely generated by the energetic tritium β-decay electrons that liberate carbon atoms from the CD capsule and the cryogenic epoxies used in the target mounts (the target and support structures are immersed in DT gas during the diffusion fill and the pressure is ramped up to hundreds of atmospheres at room temperature over a 24-h period). Since the DT fuel supply is operated as a closed loop, organics formed during a fill remain entrained in the fuel for subsequent fills.

The gases condense on the outer surface of the capsule as it is being cooled under pressure. As the temperature of the DT approaches the triple point, the DT liquefies, immersing the capsule and effectively stopping further contaminant gas condensation from the vapor phase on the outer surface. The contaminant gases are presumably on the inside of the capsule as well since the shell is quite permeable at room temperature. The gases likely form monolayers on the inner surface as the

temperature falls below the various triple points. Based on the characterization possible to date, there is no visible evidence of crystalline or condensation-related features on the inner surface of the CD shell. Any features on the inner surface would need to first feed out to the ablation surface (where the amplitudes would be quite reduced) to be associated with carbon mixing in the core (recall Fig. 135.8).

Two facility projects are underway to eliminate these "trace" gases in the fuel supply. The first is a PdAg filter[34] that passes only hydrogen into the high-pressure permeation cell with the capsules. This filter will be implemented in early 2013. The second project is an isotope separation unit that will remove all contaminants from the DT-fuel supply including protium (^{1}H). Protium forms HD, HT, and HH molecules that lower the effective triple point of the fuel, impacting layer formation and the density of the void. This system is expected to become operational in late 2013.

Experimental Ignition Threshold Factor

The goal of the National Ignition Campaign (NIC) was to demonstrate alpha heating and ignition using indirectly driven (ID) cryogenic DT implosions on the NIF.[35] Using multidimensional hydrodynamic simulations, Haan *et al.*[22] derived a convenient metric (ITFx) for tracking the relative implosion performance as capsule and drive parameters were tuned to achieve the required implosion symmetry, fuel adiabat, and implosion velocity. The ITFx is given by

$$\mathrm{ITFx}\left(\mathrm{ID}\right)=\left(Y_{\mathrm{n}}\middle/3.2\times10^{15}\right)\times\left(\mathrm{DSR}\middle/0.07\right)^{2.3},\qquad(4)$$

where DSR is the "down-scatter ratio"[36] in percent and related[37] to the total fuel areal density by ρR (g/cm^2) = 21 × DSR(%), i.e., the normalization factor of 0.07 is effectively a fuel areal density of 1.5 g/cm^2. The normalization factors on the yield and areal density are set so that an ITFx of unity implies a 50% probability that the target will ignite (given the spectrum of tolerances used in the simulations). Symmetric direct-drive (DD) implosions on OMEGA can be plotted using the ITFx(ID) on an equivalent performance basis by using the standard hydrodynamic relations[24] $\rho R \sim E_{\mathrm{L}}^{1/3}$, $Y \sim T_{\mathrm{i}}^{4.7}\times\rho R^{0.56}\times M_{\mathrm{fuel}}$, and $T \sim E^{0.07}$. The ignition Y_{n} and ρR in Eq. (4) can be replaced by laser energy and mass-scaled quantities from OMEGA cryogenic DT implosions. The OMEGA ignition-equivalent ITFx is then

$$\mathrm{ITFx}\left(\mathrm{NIF\ DD}\right)=\mathrm{ITFx}\left(\mathrm{ID}\ \Omega\right)\times\left(E_{\mathrm{NIF}}\middle/E_{\Omega}\right)^{1.28}\times\left(M_{\mathrm{NIF}}\middle/M_{\Omega}\right)\times\left(\mathrm{YOC}_{\mathrm{NIF}}\middle/\mathrm{YOC}_{\Omega}\right),\qquad(5)$$

where ITFx (ID Ω) is Eq. (4) with the OMEGA (Ω) measured quantities, E is the laser energy, M is the fuel mass, and YOC is based on an equivalent perturbation spectrum for each facility.[24] The assumption is that the YOC on the NIF will be higher than on OMEGA for an equivalent perturbation spectrum, given the larger capsule and consequent smaller perturbation wavelengths. For E_{NIF} = 1.8 MJ, E_{Ω} = 25 kJ, M_{NIF} = 0.17 mg, M_{Ω} = 0.02 mg, and $\mathrm{YOC}_{\mathrm{NIF}}$ = 50% and YOC_{Ω} = 25% (best YOC_{Ω} for an adiabat of ~3 and V_{imp} of ~350 km/s),

$$\mathrm{ITFx}\left(\mathrm{NIF\ DD}\right)=3505\times\mathrm{ITFx}\left(\mathrm{ID}\ \Omega\right).\qquad(6)$$

Figure 135.11 shows the distribution of the implosions discussed above in a plot of measured yield and ρR (as in Fig. 135.2 each point represents an experiment). The blue squares are implosions using pure-CD ablators while the orange diamonds are Si-doped ablators (typically a few atom percent of silicon in the outer few microns of the shell). The red circles are from a high-areal-density series of experiments performed in 2009 (Refs. 3 and 20). There is no discernible difference between the doped and undoped ablators, confirming the conclusion from Table 135.I that imprint alone cannot explain the current target performance. Curves of constant ITFx (NIF DD) from Eq. (6) are superimposed. The best-performing implosions on OMEGA have achieved an equivalent NIF direct-drive ITFx

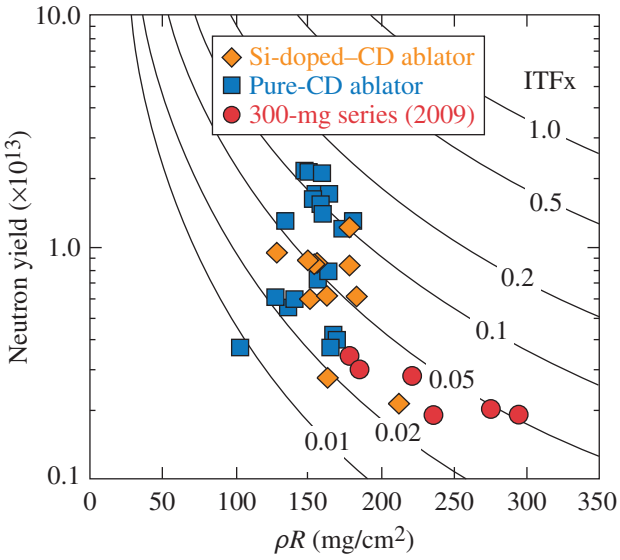

Figure 135.11
The implosions represented in Fig. 135.2 are plotted according to the measured yield and areal density. Curves of constant NIF-equivalent direct-drive ITFx [Eq. (6)] are also plotted. The blue squares are pure-CD ablators while the orange diamonds are Si-doped–CD ablators. The red circles are from a high-areal-density series of experiments performed in 2009 (Refs. 3 and 20).

of nearly 0.2 (this includes the 2× multiplier from the YOC scaling). The highest ρR to date in an OMEGA DT implosion (~295 mg/cm^2) produced an ITFx (NIF DD) nearly 3× less as a result of the low yield. An ITFx (NIF DD) of unity is satisfied for an areal density of 300 mg/cm^2 and a yield of 4×10^{13}, very similar to the values derived by Betti *et al.*[24] from the generalized Lawson criterion for ICF and discussed above.

It is apparent from Fig. 135.11 that recent experiments have not produced areal densities above 200 mg/cm^2 regardless of the design adiabat and the implosion velocity. All attempts to reduce the adiabat to increase the areal density led to a decrease in both the yield and areal densities; at an adiabat of 3, the measured yields and areal densities drop to below 10% and 50% of 1-D predictions, respectively (with ITFx values well below 0.1). This suggests that ablation-front hydrodynamic instabilities remain the leading cause of the breakup of the fuel shell in-flight.

Conclusion

The goal of the cryogenic DT implosion experiments at LLE is to demonstrate ignition hydrodynamic similarity. Recent cryogenic DT implosions on OMEGA have probed a broad region of design space that includes fuel adiabats from <2 to 4, IFAR's from <15 to more than 25, and implosion velocities from 250 to 380 km/s. Several of the targets would have demonstrated ignition hydrodynamic equivalence had the measured performance agreed with the 1-D prediction. The key to this rapid progress is the flexible symmetric direct-drive target platform on the OMEGA laser. With the peak drive intensity defined by the hydro scaling discussed in **Hydrodynamic Similarity and Experimental Design** (p. 145), the adiabat of any layered DT target can be easily changed by adjusting the laser-drive picket energies and relative timings, while the implosion velocity and IFAR are set by the mass of the ablator and ice.

The conclusion from the data and 2-D simulations is that the stability of the imploding shell is compromised by dozens of isolated outer-surface defects. These defects act as perturbation seeds that grow rapidly at the ablation surface and mix ablator material into the core. The defects that appear on the capsules following the permeation fill process are most likely caused by contaminant gases in the DT fuel supply that freeze on the surface of the capsule as it is being cooled under pressure.

High implosion velocities are achieved with higher-adiabat target designs that stabilize the hydro-instability growth at the ablation surface. At the highest adiabats (4), the measured areal density and primary neutron yield are >80% to 90% and ≥25% of the 1-D prediction, respectively. Comparable performance relative to 1-D at adiabats of 2.0 to 2.5 is needed to demonstrate ignition hydrodynamic similarity.

ACKNOWLEDGMENT

This work was supported by the U.S. Department of Energy Office of Inertial Confinement Fusion under Cooperative Agreement No. DE-FC52-08NA28302, the University of Rochester, and the New York State Energy Research and Development Authority. The support of DOE does not constitute an endorsement by DOE of the views expressed in this article.

REFERENCES

1. T. R. Boehly, D. L. Brown, R. S. Craxton, R. L. Keck, J. P. Knauer, J. H. Kelly, T. J. Kessler, S. A. Kumpan, S. J. Loucks, S. A. Letzring, F. J. Marshall, R. L. McCrory, S. F. B. Morse, W. Seka, J. M. Soures, and C. P. Verdon, Opt. Commun. **133**, 495 (1997).

2. W. J. Hogan, E. I. Moses, B. E. Warner, M. S. Sorem, and J. M. Soures, Nucl. Fusion **41**, 567 (2001).

3. V. N. Goncharov, T. C. Sangster, T. R. Boehly, S. X. Hu, I. V. Igumenshchev, F. J. Marshall, R. L. McCrory, D. D. Meyerhofer, P. B. Radha, W. Seka, S. Skupsky, C. Stoeckl, D. T. Casey, J. A. Frenje, and R. D. Petrasso, Phys. Rev. Lett. **104**, 165001 (2010).

4. P. B. Radha, F. J. Marshall, J. A. Marozas, A. Shvydky, I. Gabalski, T. R. Boehly, T. J. B. Collins, R. S. Craxton, D. H. Edgell, R. Epstein, J. A. Frenje, D. H. Froula, V. N. Goncharov, M. Hohenberger, R. L. McCrory, P. W. McKenty, D. D. Meyerhofer, R. D. Petrasso, T. C. Sangster, and S. Skupsky, Phys. Plasmas **20**, 056306 (2013).

5. S. Skupsky, J. A. Marozas, R. S. Craxton, R. Betti, T. J. B. Collins, J. A. Delettrez, V. N. Goncharov, P. W. McKenty, P. B. Radha, T. R. Boehly, J. P. Knauer, F. J. Marshall, D. R. Harding, J. D. Kilkenny, D. D. Meyerhofer, T. C. Sangster, and R. L. McCrory, Phys. Plasmas **11**, 2763 (2004).

6. S. Skupsky, R. S. Craxton, F. J. Marshall, R. Betti, T. J. B. Collins, R. Epstein, V. N. Goncharov, I. V. Igumenshchev, J. A. Marozas, P. W. McKenty, P. B. Radha, J. D. Kilkenny, D. D. Meyerhofer, T. C. Sangster, and R. L. McCrory, J. Phys. IV France **133**, 233 (2006).

7. S. X. Hu, G. Fiksel, V. N. Goncharov, S. Skupsky, D. D. Meyerhofer, and V. A. Smalyuk, Phys. Rev. Lett. **108**, 195003 (2012).

8. I. V. Igumenshchev, W. Seka, D. H. Edgell, D. T. Michel, D. H. Froula, V. N. Goncharov, R. S. Craxton, L. Divol, R. Epstein, R. Follett, J. H. Kelly, T. Z. Kosc, A. V. Maximov, R. L. McCrory, D. D. Meyerhofer, P. Michel, J. F. Myatt, T. C. Sangster, A. Shvydky, S. Skupsky, and C. Stoeckl, Phys. Plasmas **19**, 056314 (2012).

9. S. X. Hu, V. A. Smalyuk, V. N. Goncharov, J. P. Knauer, P. B. Radha, I. V. Igumenshchev, J. A. Marozas, C. Stoeckl, B. Yaakobi, D. Shvarts, T. C. Sangster, P. W. McKenty, D. D. Meyerhofer, S. Skupsky, and R. L. McCrory, Phys. Rev. Lett. **100**, 185003 (2008).

10. P. B. Radha, C. Stoeckl, V. N. Goncharov, J. A. Delettrez, D. H. Edgell, J. A. Frenje, I. V. Igumenshchev, J. P. Knauer, J. A. Marozas, R. L.

McCrory, D. D. Meyerhofer, R. D. Petrasso, S. P. Regan, T. C. Sangster, W. Seka, and S. Skupsky, Phys. Plasmas 18, 012705 (2011).

11. T. R. Boehly, V. N. Goncharov, W. Seka, M. A. Barrios, P. M. Celliers, D. G. Hicks, G. W. Collins, S. X. Hu, J. A. Marozas, and D. D. Meyerhofer, Phys. Rev. Lett. **106**, 195005 (2011).

12. V. N. Goncharov, T. C. Sangster, P. B. Radha, R. Betti, T. R. Boehly, T. J. B. Collins, R. S. Craxton, J. A. Delettrez, R. Epstein, V. Yu. Glebov, S. X. Hu, I. V. Igumenshchev, J. P. Knauer, S. J. Loucks, J. A. Marozas, F. J. Marshall, R. L. McCrory, P. W. McKenty, D. D. Meyerhofer, S. P. Regan, W. Seka, S. Skupsky, V. A. Smalyuk, J. M. Soures, C. Stoeckl, D. Shvarts, J. A. Frenje, R. D. Petrasso, C. K. Li, F. Séguin, W. Manheimer, and D. G. Colombant, Phys. Plasmas **15**, 056310 (2008).

13. S. X. Hu, V. Smalyuk, V. N. Goncharov, S. Skupsky, T. C. Sangster, D. D. Meyerhofer, and D. Shvarts, Phys. Rev. Lett. **101**, 055002 (2008).

14. B. Yaakobi, P.-Y. Chang, A. A. Solodov, C. Stoeckl, D. H. Edgell, R. S. Craxton, S. X. Hu, J. F. Myatt, F. J. Marshall, W. Seka, and D. H. Froula, Phys. Plasmas **19**, 012704 (2012).

15. V. N. Goncharov, J. P. Knauer, P. W. McKenty, P. B. Radha, T. C. Sangster, S. Skupsky, R. Betti, R. L. McCrory, and D. D. Meyerhofer, Phys. Plasmas **10**, 1906 (2003).

16. P. B. Radha, J. A. Marozas, F. J. Marshall, A. Shvydky, T. J. B. Collins, V. N. Goncharov, R. L. McCrory, P. W. McKenty, D. D. Meyerhofer, T. C. Sangster, and S. Skupsky, Phys. Plasmas **19**, 082704 (2012).

17. C. Stoeckl, C. Chiritescu, J. A. Delettrez, R. Epstein, V. Yu. Glebov, D. R. Harding, R. L. Keck, S. J. Loucks, L. D. Lund, R. L. McCrory, P. W. McKenty, F. J. Marshall, D. D. Meyerhofer, S. F. B. Morse, S. P. Regan, P. B. Radha, S. Roberts, T. C. Sangster, W. Seka, S. Skupsky, V. A. Smalyuk, C. Sorce, J. M. Soures, R. P. J. Town, J. A. Frenje, C. K. Li, R. D. Petrasso, F. H. Séguin, K. Fletcher, S. Padalino, C. Freeman, N. Izumi, R. Lerche, and T. W. Phillips, Phys. Plasmas **9**, 2195 (2002).

18. T. C. Sangster, R. Betti, R. S. Craxton, J. A. Delettrez, D. H. Edgell, L. M. Elasky, V. Yu. Glebov, V. N. Goncharov, D. R. Harding, D. Jacobs-Perkins, R. Janezic, R. L. Keck, J. P. Knauer, S. J. Loucks, L. D. Lund, F. J. Marshall, R. L. McCrory, P. W. McKenty, D. D. Meyerhofer, P. B. Radha, S. P. Regan, W. Seka, W. T. Shmayda, S. Skupsky, V. A. Smalyuk, J. M. Soures, C. Stoeckl, B. Yaakobi, J. A. Frenje, C. K. Li, R. D. Petrasso, F. H. Séguin, J. D. Moody, J. A. Atherton, B. D. MacGowan, J. D. Kilkenny, T. P. Bernat, and D. S. Montgomery, Phys. Plasmas **14**, 058101 (2007).

19. T. C. Sangster, V. N. Goncharov, P. B. Radha, V. A. Smalyuk, R. Betti, R. S. Craxton, J. A. Delettrez, D. H. Edgell, V. Yu. Glebov, D. R. Harding, D. Jacobs-Perkins, J. P. Knauer, F. J. Marshall, R. L. McCrory, P. W. McKenty, D. D. Meyerhofer, S. P. Regan, W. Seka, R. W. Short, S. Skupsky, J. M. Soures, C. Stoeckl, B. Yaakobi, D. Shvarts, J. A. Frenje, C. K. Li, R. D. Petrasso, and F. H. Séguin, Phys. Rev. Lett. **100**, 185006 (2008).

20. T. C. Sangster, V. N. Goncharov, R. Betti, T. R. Boehly, D. T. Casey, T. J. B. Collins, R. S. Craxton, J. A. Delettrez, D. H. Edgell, R. Epstein, K. A. Fletcher, J. A. Frenje, V. Yu. Glebov, D. R. Harding, S. X. Hu, I. V. Igumenshchev, J. P. Knauer, S. J. Loucks, C. K. Li, J. A. Marozas, F. J. Marshall, R. L. McCrory, P. W. McKenty, D. D. Meyerhofer, P. M. Nilson, S. P. Padalino, R. D. Petrasso, P. B. Radha, S. P. Regan, F. H. Seguin, W. Seka, R. W. Short, D. Shvarts, S. Skupsky, V. A. Smalyuk, J. M. Soures, C. Stoeckl, W. Theobald, and B. Yaakobi, Phys. Plasmas **17**, 056312 (2010).

21. P. B. Radha, R. Betti, T. R. Boehly, J. A. Delettrez, D. H. Edgell, V. N. Goncharov, I. V. Igumenshchev, J. P. Knauer, J. A. Marozas, F. J. Marshall, R. L. McCrory, D. D. Meyerhofer, S. P. Regan, T. C. Sangster, W. Seka, S. Skupsky, A. A. Solodov, C. Stoeckl, W. Theobald, J. A. Frenje, D. T. Casey, C. K. Li, and R. D. Petrasso, IEEE Trans. Plasma Sci. **39**, 1007 (2011).

22. S. W. Haan, J. D. Lindl, D. A. Callahan, D. S. Clark, J. D. Salmonson, B. A. Hammel, L. J. Atherton, R. C. Cook, M. J. Edwards, S. Glenzer, A. V. Hamza, S. P. Hatchett, M. C. Herrmann, D. E. Hinkel, D. D. Ho, H. Huang, O. S. Jones, J. Kline, G. Kyrala, O. L. Landen, B. J. MacGowan, M. M. Marinak, D. D. Meyerhofer, J. L. Milovich, K. A. Moreno, E. I. Moses, D. H. Munro, A. Nikroo, R. E. Olson, K. Peterson, S. M. Pollaine, J. E. Ralph, H. F. Robey, B. K. Spears, P. T. Springer, L. J. Suter, C. A. Thomas, R. P. Town, R. Vesey, S. V. Weber, H. L. Wilkens, and D. C Wilson, Phys. Plasmas **18**, 051001 (2011).

23. C. D. Zhou and R. Betti, Phys. Plasmas **15**, 102707 (2008).

24. R. Betti, presented at the 24th IAEA Fusion Energy Conference, San Diego, CA, 8–13 October 2012.

25. H. A. Baldis and C. J. Walsh, Phys. Fluids **26**, 1364 (1983).

26. J. Delettrez, R. Epstein, M. C. Richardson, P. A. Jaanimagi, and B. L. Henke, Phys. Rev. A **36**, 3926 (1987).

27. R. A. Lerche, D. W. Phillion, and G. L. Tietbohl, Rev. Sci. Instrum. **66**, 933 (1995).

28. R. Betti, P. Y. Chang, B. K. Spears, K. S. Anderson, J. Edwards, M. Fatenejad, J. D. Lindl, R. L. McCrory, R. Nora, and D. Shvarts, Phys. Plasmas **17**, 058102 (2010).

29. P. B. Radha, T. J. B. Collins, J. A. Delettrez, Y. Elbaz, R. Epstein, V. Yu. Glebov, V. N. Goncharov, R. L. Keck, J. P. Knauer, J. A. Marozas, F. J. Marshall, R. L. McCrory, P. W. McKenty, D. D. Meyerhofer, S. P. Regan, T. C. Sangster, W. Seka, D. Shvarts, S. Skupsky, Y. Srebro, and C. Stoeckl, Phys. Plasmas **12**, 056307 (2005).

30. J. A. Frenje, K. M. Green, D. G. Hicks, C. K. Li, F. H. Séguin, R. D. Petrasso, T. C. Sangster, T. W. Phillips, V. Yu. Glebov, D. D. Meyerhofer, S. Roberts, J. M. Soures, C. Stoeckl, K. Fletcher, S. Padalino, and R. J. Leeper, Rev. Sci. Instrum. **72**, 854 (2001).

31. C. J. Forrest, P. B. Radha, V. Yu. Glebov, V. N. Goncharov, J. P. Knauer, A. Pruyne, M. Romanofsky, T. C. Sangster, M. J. Shoup III, C. Stoeckl, D. T. Casey, M. Gatu-Johnson, and S. Gardner, Rev. Sci. Instrum. **83**, 10D919 (2012).

32. J. A. Frenje, C. K. Li, F. H. Séguin, D. T. Casey, R. D. Petrasso, D. P. McNabb, P. Navratil, S. Quaglioni, T. C. Sangster, V. Yu. Glebov, and D. D. Meyerhofer, Phys. Rev. Lett. **107**, 122502 (2011).

33. V. A. Smalyuk, V. N. Goncharov, K. S. Anderson, R. Betti, R. S. Craxton, J. A. Delettrez, D. D. Meyerhofer, S. P. Regan, and T. C. Sangster, Phys. Plasmas **14**, 032702 (2007).

34. H. Amandusson, L.-G. Ekedahl, and H. Dannetun, J. Membr. Sci. **193**, 35 (2001).

35. J. D. Lindl and E. I. Moses, Phys. Plasmas **18**, 050901 (2011).

36. J. A. Frenje, D. T. Casey, C. K. Li, J. R. Rygg, F. H. Séguin, R. D. Petrasso, V. Yu. Glebov, D. D. Meyerhofer, T. C. Sangster, S. Hatchett, S. Haan, C. Cerjan, O. Landen, M. Moran, P. Song, D. C. Wilson, and R. J. Leeper, Rev. Sci. Instrum. **79**, 10E502 (2008).

37. A. J. Mackinnon, J. L. Kline, S. N. Dixit, S. H. Glenzer, M. J. Edwards, D. A. Callahan, N. B. Meezan, S. W. Haan, J. D. Kilkenny, T. Döppner, D. R. Farley, J. D. Moody, J. E. Ralph, B. J. MacGowan, O. L. Landen, H. F. Robey, T. R. Boehly, P. M. Celliers, J. H. Eggert, K. Krauter, G. Frieders, G. F. Ross, D. G. Hicks, R. E. Olson, S. V. Weber, B. K. Spears, J. D. Salmonsen, P. Michel, L. Divol, B. Hammel, C. A. Thomas, D. S. Clark, O. S. Jones, P. T. Springer, C. J. Cerjan, G. W. Collins, V. Y. Glebov, J. P. Knauer, C. Sangster, C. Stoeckl, P. McKenty, J. M. McNaney, R. J. Leeper, C. L. Ruiz, G. W. Cooper, A. G. Nelson, G. G. A. Chandler, K. D. Hahn, M. J. Moran, M. B. Schneider, N. E. Palmer, R. M. Bionta, E. P. Hartouni, S. LePape, P. K. Patel, N. Izumi, R. Tommasini, E. J. Bond, J. A. Caggiano, R. Hatarik, G. P. Grim, F. E. Merrill, D. N. Fittinghoff, N. Guler, O. Drury, D. C. Wilson, H. W. Herrmann, W. Stoeffl, D. T. Casey, M. G. Johnson, J. A. Frenje, R. D. Petrasso, A. Zylestra, H. Rinderknecht, D. H. Kalantar, J. M. Dzenitis, P. Di Nicola, D. C. Eder, W. H. Courdin, G. Gururangan, S. C. Burkhart, S. Friedrich, D. L. Blueuel, L. A. Bernstein, M. J. Eckart, D. H. Munro, S. P. Hatchett, A. G. Macphee, D. H. Edgell, D. K. Bradley, P. M. Bell, S. M. Glenn, N. Simanovskaia, M. A. Barrios, R. Benedetti, G. A. Kyrala, R. P. J. Town, E. L. Dewald, J. L. Milovich, K. Widmann, A. S. Moore, G. LaCaille, S. P. Regan, L. J. Suter, B. Felker, R. C. Ashabranner, M. C. Jackson, R. Prasad, M. J. Richardson, T. R. Kohut, P. S. Datte, G. W. Krauter, J. J. Klingman, R. F. Burr, T. A. Land, M. R. Hermann, D. A. Latray, R. L. Saunders, S. Weaver, S. J. Cohen, L. Berzins, S. G. Brass, E. S. Palma, R. R. Lowe-Webb, G. N. McHalle, P. A. Arnold, L. J. Lagin, C. D. Marshall, G. K. Brunton, D. G. Mathisen, R. D. Wood, J. R. Cox, R. B. Ehrlich, K. M. Knittel, M. W. Bowers, R. A. Zacharias, B. K. Young, J. P. Holder, J. R. Kimbrough, T. Ma, K. N. La Fortune, C. C. Widmayer, M. J. Shaw, G. V. Erbert, K. S. Jancaitis, J. M. DiNicola, C. Orth, G. Heestand, R. Kirkwood, C. Haynam, P. J. Wegner, P. K. Whitman, A. Hamza, E. G. Dzenitis, R. J. Wallace, S. D. Bhandarkar, T. G. Parham, R. Dylla-Spears, E. R. Mapoles, B. J. Kozioziemski, J. D. Sater, C. F. Walters, B. J. Haid, J. Fair, A. Nikroo, E. Giraldez, K. Moreno, B. Vanwonterghem, R. L. Kauffman, S. Batha, D. W. Larson, R. J. Fortner, D. H. Schneider, J. D. Lindl, R. W. Patterson, L. J. Atherton, and E. I. Moses, Phys. Rev. Lett. **108**, 215005 (2012).